Research Square

Preprints are preliminary reports that have not undergone peer review.
They should not be considered conclusive, used to inform clinical practice,
or referenced by the media as validated information.

Comparative Clinical and Biomechanical Assessment of Patient-Specific 3D-Printed Monoblock Versus Commercial Modular Acetabular Prostheses in Hip Arthroplasty for Reconstruction of Severe Acetabular Bone Defects

Zhiwen Dong
Nanjing First Hospital
Peiran Wei
Nanjing First Hospital
Xiangyang Xu
Southeast University
Bianba Ciren
People's Hospital of Mozhugongka County
Weihang Zhu
Nanjing First Hospital
Wenhui Hu
Nanjing First Hospital
Mengtao Wang
Nanjing First Hospital
Zhicheng Cao
Nanjing First Hospital
Liming Wang
Nanjing First Hospital
Cheng Tang
tangc233@njmu.edu.cn

Nanjing First Hospital

Research Article

Keywords: Patient-specific, 3D-printed monoblock prosthesis, Acetabular bone defect, Modular prosthesis, Biomechanics

Posted Date: November 4th, 2026

DOI: https://doi.org/10.21203/rs.3.rs-11365327/v1

License: This work is licensed under a Creative Commons Attribution 4.0 International License.
Read Full License

Additional Declarations: No competing interests reported.

Abstract

Background

Commercial modular acetabular prostheses are widely used to reconstruct severe acetabular defects in hip arthroplasty. However, modular techniques may be limited by suboptimal defect matching and technical complexity. Patient-specific 3D-printed monoblock acetabular prostheses represent a novel reconstructive strategy that enables precise bone defect matching, customized fixation and facilitates restoration of the hip center of rotation. Nevertheless, clinical and biomechanical evidence regarding these prostheses remains limited. This study aimed to compare the clinical outcomes and biomechanical behavior of patient-specific 3D-printed monoblock prostheses with those of commercial modular prostheses.

Methods

Thirty-five patients with Paprosky type II–III acetabular defects were retrospectively divided into a 3D-printed group (n = 17) and a modular group (n = 18). Clinical outcomes and radiographic parameters were compared between groups. Biomechanical evaluations combining cadaveric testing and finite element analysis (FEA) were performed using cadaveric Paprosky type IIIA acetabular defect models.

Results

At a mean follow-up of approximately 32 months, the 3D-printed group had higher Harris hip scores (82.8 ± 6.1 vs. 76.6 ± 5.2, $p = 0.003$) and lower visual analogue scale pain scores (median 1 [interquartile range 0.5–1.5] vs. 2 [1–2], $p = 0.003$). The 3D-printed group also showed more accurate restoration of the vertical and horizontal positions of the hip center of rotation ($p = 0.016$ and 0.045), less leg-length discrepancy (3.1 ± 1.8 vs. 6.2 ± 2.9 mm, $p < 0.001$), and a smaller femoral offset difference (3.3 ± 2.2 vs. 5.1 ± 1.2 mm, $p = 0.006$). At 800 cycles, permanent migration (86 [82–94] vs. 181 [178–186] μm, $p < 0.001$) and inducible micromotion (126 [119–128] vs. 289 [248–296] μm, $p < 0.001$) were markedly lower for the 3D-printed prostheses. The monoblock prostheses exhibited higher periacetabular bone strain and a more even prosthetic stress distribution than the modular prostheses, as demonstrated by cadaveric strain measurement and FEA, respectively.

Conclusions

Patient-specific 3D-printed monoblock acetabular prostheses were associated with better clinical outcomes and more accurate anatomical reconstruction than commercial modular acetabular prostheses. Independent biomechanical analyses suggested improved initial stability and more favorable periacetabular load transfer with monoblock prostheses.

1. Introduction

With the aging of the population, the number of total hip arthroplasty (THA) procedures performed annually continues to increase, accompanied by a corresponding rise in revision surgeries due to prosthesis loosening, infection, dislocation, and other complications [1]. Revision hip surgery is technically demanding because it requires the reconstruction of bone defects, the restoration of the hip joint's center of rotation (COR), and the achievement of durable initial stability. Among these challenges, the reconstruction of severe acetabular bone defects, most commonly classified as Paprosky type II or III defects [2], remains one of the most difficult aspects in revision THA.

Various clinical techniques are used for acetabular reconstruction, and these include impacted bone grafting, modular acetabular prostheses, acetabular reinforcement rings, “cup-cage” technique, double cups, and jumbo cups [3–7]. However, each technique has inherent limitations. Although commercial modular acetabular prostheses are widely used to reconstruct severe acetabular defects, their standardized shapes and sizes may result in a poor fit within irregular defects, complicating implantation and compromising initial stability. Moreover, fracture or loosening of the augments may lead to construct failure [8–10]. Structural allografts are susceptible to bone resorption and limited osseous ingrowth, which may prevent the formation of a stable foundation for long-term fixation [11]. The "cup-cage" technique provides initial mechanical stability through the cage, whereas long-term fixation depends on biological ingrowth into the cup; nevertheless, the reported 15-year survivorship free from all-cause failure is only 69.8% [12].

With advances in digital technology and medical engineering, patient-specific 3D-printed monoblock prostheses designed from preoperative imaging data have emerged as a promising alternative. By addressing the fundamental mismatch between standardized implants and irregular host bone, these prostheses enable personalized reconstruction and customized fixation, thereby maximizing the preservation and utilization of host bone while facilitating restoration of the hip COR [13–15]. However, direct comparative evidence comparing patient-specific 3D-printed monoblock with commercial modular acetabular prostheses in hip arthroplasty remains limited, particularly evidence integrating clinical outcomes with biomechanical validation. This study therefore aimed to (1) compare the clinical outcomes of 3D-printed monoblock and commercial modular acetabular prostheses used to reconstruct severe acetabular bone defects; and (2) compare the biomechanical behavior under cyclic loading using cadaveric testing and FEA.

2. Methods

2.1. General Information

We conducted a retrospective comparative study at a tertiary academic hospital. The study protocol was reviewed and approved by the institutional Ethics Committee and conducted in accordance with the principles of the Declaration of Helsinki. Detailed ethical information, including the consent procedures

for the clinical and cadaveric components, is provided in the Ethics statement. We reviewed the medical records of all patients who had undergone THA between June 2015 and December 2024.

During this period, we initially identified 57 patients (57 hips) with severe acetabular bone defects (Paprosky classification ≥ II). The inclusion criteria were as follows: (1) THA performed for advanced hip disorders, including traumatic arthritis, developmental hip dysplasia, or aseptic implant loosening; (2) preoperative imaging confirming Paprosky type II or more severe acetabular defects requiring reconstruction with structural components; and (3) a minimum of 1 year of complete clinical and radiographic follow-up data. Patients were excluded if they had (1) a history of or current diagnosis of benign or malignant acetabular tumors; (2) preoperative or intraoperative evidence of pelvic discontinuity; (3) severe neuromuscular or psychiatric conditions precluding cooperation with rehabilitation and follow-up; or (4) incomplete follow-up data. Following the application of these criteria, a total of 35 patients (35 hips) were ultimately enrolled.

Patients were divided into the 3D-printed group (n = 17) and the modular group (n = 18) according to the type of prosthesis implanted. Both surgical techniques were well established at our institution, and both prosthetic systems were routinely and concurrently available. Treatment allocation was determined through shared decision-making between the surgeon and the patient. All procedures were performed by a single senior surgical team. Baseline characteristics recorded preoperatively (age, sex, BMI, and acetabular defect classification) were statistically compared between the two groups, revealing no significant differences and thus confirming adequate comparability (Table 1).

Table 1
Basic characteristics of the 3D-printed group and the modular group

Parameter	**3D-printed group** **n = 17**	**Modular group** **n = 18**	***p*-Value**
Gender			0.505
Female	9 (52.9)	7 (38.9)	
Male	8 (47.1)	11 (61.1)	
Height (cm)	161.0 ± 8.0	162.2 ± 6.4	0.632
Weight (kg)	59.3 ± 7.6	62.9 ± 4.5	0.095
BMI (kg/m^2)	23.0 ± 2.9	24.0 ± 1.6	0.228
Age (years)	64.1 ± 10.4	62.5 ± 9.0	0.626
Range (years)	51–86	45–77	
Laterality			0.489
Right	5 (29.4)	8 (44.4)	
Left	12 (70.6)	10 (55.6)	
Surgery duration (minutes)	202.4 ± 55.6	206.0 ± 56.5	0.848
Average follow-up time (months)	32.7 ± 6.8	31.7 ± 11.6	0.763
Range (months)	22.0–45.7	13.2–53.6	
Paprosky grade			0.694
IIA	4 (23.5)	3 (16.7)	
IIC	3 (17.6)	5 (27.8)	
IIIA	5 (29.4)	7 (38.9)	
IIIB	5 (29.4)	3 (16.7)	
Reason for surgery			0.441
Aseptic loosening	14 (82.4)	14 (77.8)	
Developmental hip dysplasia	1 (5.9)	0 (0)	
Acetabular fracture	2 (11.8)	4 (22.2)	

BMI, body mass index (calculated as weight in kg divided by height in m^2). Data are given as mean ± SD or n (%)

In the 3D-printed group, a custom-designed, patient-specific titanium alloy prosthesis, fabricated using preoperative computed tomography (CT) data, was implanted (Fig. 1). In the modular group, reconstruction was performed using a commercially available modular augment and cup system. Representative preoperative and postoperative radiographs comparing the two reconstruction methods are shown in Fig. 2.

2.2. Preoperative Preparation

2.2.1. The 3D-printed Group

For patients in the 3D-printed group, preoperative thin-layer CT scans of both pelves were performed using a 64-slice spiral CT scanner (Siemens AG, Munich, Germany). The scanned data were stored and exported in DICOM format. Then, they were imported into Mimics 17.0 (Materialise, Leuven, Belgium), where bony structures were segmented and reconstructed via thresholding based on CT Hounsfield units (148–661 for cancellous bone; 662–1988 for cortical bone), supplemented by manual correction to eliminate metallic artifacts. Three-dimensional models of the pelvis and acetabular cup prosthesis were subsequently generated and exported in STL format.

The STL models were then imported into 3-Matic software (Materialise), where the contralateral mirror-image technique was employed to restore the anatomical reference for the hip rotation center on the affected side. Based on the patient-specific acetabular defect morphology and residual bony anatomy, customized flanged acetabular components were designed to precisely reconstruct the bone defect, maximize osseous containment by the residual host bone, and optimize the host-prosthesis contact area. Additionally, the spatial configuration and insertion trajectories of the flange and fixation screws were preoperatively determined according to local bone stock quality, thereby enhancing primary stability.

Finally, the acetabular prosthesis model data were transferred to a 3D printer. The 3D-printed monoblock prosthesis was fabricated as an integrated construct via electron beam melting (EBM) using an Arcam Q10 system (Arcam AB, Sweden) with medical-grade Ti6Al4V powder (b-ONE ORTHO, Corp.). The implant featured a porous surface with a thickness of 1.8 mm, characterized by a pore size of 0.60–0.65 mm, a strut diameter of 0.50–0.60 mm, and a porosity of 65%–70%. In accordance with the preoperative design specifications, complementary fixation screws were machined from Ti6Al4V alloy (Baoji Titanium Industry Co., Ltd., China). The prostheses and their design processes are displayed in Figs. 1 and 3, as well as in the supplementary materials (Figs. S1-S3).

2.2.2. The Modular Group

The modular group utilized X-ray films and CT scans for preoperative planning. The surgeon precisely planned the position and size of the prosthesis through imaging data. With the help of plastic templates provided by the manufacturer, an appropriate acetabular prosthesis model was selected to fully fill the

acetabulum and maintain adequate coverage. Once the implant design was finalized, the types and sizes of the selected acetabular cup and augments (Beijing Chunlizhengda Medical Instruments Co., Ltd.) were preliminarily recorded, pending potential intraoperative adjustments.

2.3. Surgical Method

All surgeries were conducted by the same experienced surgical team. After the patients received general anesthesia, they were positioned in the contralateral decubitus position, and the hip joint was exposed via a standard lateral approach. Intraoperatively, fibrous scar tissue, hyperplastic joint capsules, and surrounding osteophytes were meticulously excised to fully expose the acetabulum. For patients undergoing reconstruction of bone defects with commercial modular acetabular prostheses, the true and false acetabular positions were enlarged to the preoperatively planned size using an acetabular reamer. The augments were selected and positioned in accordance with the preoperative planning and the specific intraoperative conditions, followed by the insertion of screws to ensure fixation. Bone cement was applied between the augment and the acetabular cup, and the cup was then implanted at 40–45° of abduction and 10–15° of anteversion. For patients undergoing reconstruction of bone defects with a 3D-printed monoblock prosthesis, the acetabular fossa was initially contoured to the predetermined dimensions using an acetabular rasp. The 3D-printed monoblock prosthesis was subsequently placed, and screws were inserted in the predetermined trajectory. The acetabular reconstruction was completed with the implantation of a cemented polyethylene liner. The treatment protocol for the femoral stem component remained uniform across all of the cases. A femoral head of matching size was then implanted. Subsequently, the hip joint was reduced, and its stability and range of motion were carefully evaluated. The surgical site was irrigated; a drainage tube was placed within the joint cavity; and the incision was closed layer by layer. Sterile dressings were applied to complete the procedure.

2.4. Postoperative Management

Postoperative management typically included analgesia, infection prevention, and anticoagulation. The patients were guided to follow a standardized postoperative hip joint rehabilitation protocol.

2.5. Follow-up and Observation Indicators

Follow-up was conducted at 6 weeks, 3 months, and 6 months postoperatively in the outpatient clinic, followed by annual follow-ups thereafter. Anteroposterior and lateral X-rays of the pelvis were taken at each follow-up. To ensure the objectivity and impartiality of the evaluation, all clinical and imaging data of the patients were collected and analyzed by two independent researchers who were not involved in the surgical treatment. In the event of discrepancies in the evaluation results, a consensus was reached through discussion. Clinical outcome assessment was primarily completed through quantitative analysis of hip joint function and pain level. The Harris hip score (HHS) served as the primary clinical end point for assessing hip joint function, and the visual analogue scale (VAS) for pain assessment served as a secondary clinical end point. The score data were compared between the preoperative point and the last postoperative follow-up. Radiographic outcomes were assessed on standardized anteroposterior pelvic

radiographs. Measurements were performed on DICOM images using the institutional PACS (PROTOSS PACS, Xingling Technology, Hefei, China). Linear parameters were recorded to 0.1 mm. Reliability metrics (ICC, SEM, and SDD) are provided in Supplementary Table S1. The position of the COR was assessed as follows. A horizontal reference line was drawn through the lowest points of the bilateral tear drops, and a vertical line was drawn through the lowest point of the tear drop on each side. The horizontal and vertical distances from the COR to the tear drop were measured separately on the operated side and the contralateral side, and the absolute difference between the two sides was recorded as the COR deviation. Leg length discrepancy was determined by drawing a horizontal line through the lowest points of the bilateral ischial tuberosities and a vertical line from the lowest point of the lesser trochanter of the femur to this line. The absolute difference in the lengths of these vertical lines defined the discrepancy. Femoral offset difference was defined as the variation in the vertical distance from the hip joint's COR to the longitudinal axis of the ipsilateral femoral shaft between the two sides. The fixation status and survival of the prosthesis were systematically evaluated by comparing the serial X-rays at the immediate postoperative and all follow-up time points. Specific indicators included the following: assessing the lucency lines around the acetabular cup in line with the DeLee and Charnley classification; defining any linear displacement of ≥ 2 mm in any direction or an angular change of ≥ 5° as clinically significant prosthesis migration; and diagnosing aseptic loosening and osteolysis based on established criteria.

2.6. Biomechanical Testing of Cadaveric Pelves

2.6.1. Preparation of Cadaveric Pelves

Five formalin-fixed cadaveric pelvis specimens from donors who had consented to the use of their bodies for teaching and research were obtained from our institution (see Ethics statement). Their demographic and densitometric characteristics are summarized in Table S2. Prior to the experiment, the cadaveric pelves were wrapped in saline-soaked gauze to maintain tissue hydration. To expose the anatomical landmarks necessary for surgery, we removed the soft tissue surrounding the acetabulum. All of the specimens underwent CT scans with a slice thickness of 0.625 mm and standard X-ray examinations to rule out pathological conditions such as tumors, metastatic diseases, osteoporosis, or fractures. To simulate the common clinical scenarios encountered during acetabular revision surgery, we selected Paprosky IIIA type bone defect models. To ensure high consistency in the shape of the defects on both sides, we designed 3D-printed bilateral symmetrical bone defect guiding templates based on preoperative CT data and performed bone resection with the assistance of these guiding templates. After defect creation and implantation, the pelvis was scanned again with a slice thickness of 0.625 mm, and X-ray radiography was performed to confirm the preparation with the abovementioned methods. The two prosthetic systems were randomly allocated to either the right or left hemipelvis, with a 3D-printed monoblock prosthesis implanted on one side and commercial modular acetabular prostheses implanted on the contralateral side for comparison. All prostheses were implanted at 40–45° of abduction and 10–15° of anteversion. X-rays and CT scans were taken immediately after implantation to confirm the position of the prostheses. Figure 4 illustrates the creation of the bone defects and the implantation of the two prosthetic systems.

2.6.2. Mechanical Testing

To quantify the relative micromotion between the acetabular bone surface and the prosthesis during loading, reflective markers were tracked using a calibrated stereo-3D-DIC system (Southeast University, China; U = 3.3 μm, k = 2) (Fig. 5). Detailed hardware and acquisition parameters are provided in Supplementary Table S3. The hemipelvis allocated to the monoblock prosthesis was marked at the prosthesis–bone interface, whereas the contralateral hemipelvis allocated to commercial modular acetabular prostheses was marked at the augment–bone and cup–bone interfaces. After implanting the prosthesis, the pelvis was embedded in polymer resin and positioned using anatomical landmarks such as the bilateral anterior superior iliac spines, pubic symphysis, and sacral promontory to establish a repeatable reference coordinate system on a specialized mechanical testing machine and fix it in place. To simulate the force conditions during heel strike, we combined Perry's gait parameters with Bergmann et al.'s hip joint resultant vector data, ultimately positioning the pelvis at 9° flexion in the sagittal plane and 7° abduction in the coronal plane (Fig. 5) [16, 17]. The applied load was referenced from Bergmann et al.'s measured dataset. Following Beckmann's research, we selected two levels of load range to simulate the early partial weight-bearing condition of patients after hip arthroplasty, namely 3%–30% (50–500 N) and 5%–50% (84–840 N) of the maximum resultant force during walking (Fig. 5) [18]. In line with the description from Thomas et al., we symmetrically attached resistance strain gauges to the main force area on both sides of the acetabular roof. Before the formal test, we used a 3D load sensor instead of the implant for system calibration and pretesting (Fig. 5) [19]. Through the optical measurement system, we recorded the three-dimensional displacement of each marker, and the resultant relative micromotion at each bone–prosthesis interface was calculated from the x, y, and z displacement components [20]. We defined the displacement change during the loading process as inducible micromotion (interface micromotion) and the displacement relative to the initial position after each loading stage as permanent migration (initial subsidence). During 0–600 cycles, a load of 3%–30% (50–500 N) of the maximum resultant force during walking was applied to the acetabulum at a frequency of 0.4 Hz. During 601–800 cycles, a load of 5%–50% (84–840 N) of the maximum resultant force during walking was applied to the acetabulum at a frequency of 0.25 Hz. The cyclical load was stopped every 200 cycles, and the load was maintained at 50 N for 5 min before continuing the cyclical load. The optical markers were measured repeatedly at a frequency of 1 Hz throughout the entire process. The cyclic strain changes at the strain gauge placement position were measured under the two levels of loads. To complement the cadaveric experiments, a finite element model was developed from the post-implantation CT scans (0.625 mm) of the specimen whose bone mineral density was closest to the median of the five specimens. Bone and implant geometries were segmented in Mimics 17.0 and rigidly assembled in 3-Matic. The finite element model was meshed with C3D4 elements at an average size of 1 mm. Material properties were assumed to be homogeneous, isotropic, and linearly elastic. The elastic modulus and Poisson's ratio of each material are listed in Table S4. Consistent with prior finite element studies of bone–prosthesis interfaces [9, 21], a friction coefficient of 0.8 was defined, with tied constraints applied to selected interfaces. Fixed boundary conditions were imposed on the pubis and ilium, and loads were applied at the femoral head center of rotation.

2.7. Statistical Methods

Statistical analyses were performed using SPSS 25.0 (IBM Corp., Armonk, NY, USA). Normality was assessed using the Shapiro–Wilk test. Normally distributed data are presented as mean ± standard deviation (SD) and were compared between groups using the independent-samples t test; non-normally distributed data (VAS) are presented as median (interquartile range, IQR) and were compared using the Mann–Whitney U test. Between-group comparisons were performed separately for preoperative data and for data at the last follow-up. Categorical variables are presented as frequency (percentage) and were compared using the chi-squared test or Fisher's exact test, as appropriate.

Biomechanical data are presented as median (IQR) and were obtained from contralateral hemipelves of the same specimens (paired design). The primary biomechanical endpoints were permanent migration and inducible micromotion at 800 cycles. Between-system comparisons were performed using linear mixed-effects models with specimen as a random intercept (fixed effects: group, cycle or load stage, and their interaction); estimates are reported as β with 95% confidence intervals (CI) and standardized effect size d. As a sensitivity analysis, within-specimen differences at 800 cycles were compared using the Wilcoxon signed-rank exact test. The modular augment–bone interface, peak acetabular bone strains and the finite element results are reported descriptively. All statistical tests were two-sided, and $p < 0.05$ was considered statistically significant.

3. Results

3.1. Surgical Outcomes and Complications

All surgeries were successfully completed. There were no significant differences in operation time (3D-printed group vs. modular group: 202.4 ± 55.6 min vs. 206.0 ± 56.5 min, $p > 0.05$) and follow-up time (32.7 ± 6.8 months vs. 31.7 ± 11.6 months, $p > 0.05$) between the two groups (Table 1). During the follow-up period, no complications such as prosthesis loosening, dislocation, or infection were reported in either group.

3.2. Clinical Functional Evaluation

At the last follow-up, both groups showed marked improvements in HHS and reductions in VAS compared with preoperative levels. Inter-group comparison revealed that the HHS at the last follow-up was significantly higher in the 3D-printed group than in the modular group (82.8 ± 6.1 vs. 76.6 ± 5.2, $p = 0.003$), while the VAS was significantly lower in the 3D-printed group (1 [0.5–1.5] vs. 2 [1–2], $p = 0.003$) (Tables 2 and 3).

Table 2
Preoperative data of the 3D-printed group and the modular group

Parameter	3D-printed group n = 17	Modular group n = 18	t/Z Value	*p*-Value
LLD	20.7 ± 12.4	21.9 ± 11.3	-0.30	0.766
FOD	7.8 ± 4.8	8.7 ± 3.3	-0.65	0.520
COR				
Horizontal deviation	8.2 ± 6.6	8.9 ± 5.4	-0.34	0.733
Vertical deviation	20.3 ± 14.3	21.9 ± 7.9	-0.42	0.678
HHS	36.5 ± 11.3	37.8 ± 6.4	-0.44	0.667
VAS	7 (6–7)	7 (6–7)	-0.70	0.484

LLD, Leg Length Discrepancy; FOD, Femoral Offset Difference; COR, Center of Rotation; HHS, Harris hip score (range 0–100 from worse to best); VAS, visual analogue scale (range 0–10 from best to worse). Data are given as mean ± SD or median (interquartile range)

Table 3
Postoperative data of the 3D-printed group and the modular group

Parameter	3D-printed group n = 17	Modular group n = 18	t/Z Value	*p*-Value
LLD	3.1 ± 1.8	6.2 ± 2.9	-3.79	< 0.001
FOD	3.3 ± 2.2	5.1 ± 1.2	-3.03	0.006
COR				
Horizontal deviation	3.9 ± 2.4	5.3 ± 1.5	-2.09	0.045
Vertical deviation	2.9 ± 1.4	4.0 ± 1.1	-2.59	0.014
HHS	82.8 ± 6.1	76.6 ± 5.2	3.23	0.003
VAS	1 (0.5–1.5)	2 (1–2)	-2.93	0.003

LLD, Leg Length Discrepancy; FOD, Femoral Offset Difference; COR, Center of Rotation; HHS, Harris hip score (range 0–100 from worse to best); VAS, visual analogue scale (range 0–10 from best to worse). Data are given as mean ± SD or median (interquartile range)

3.3. Imaging Anatomical Reconstruction Accuracy

In terms of the restoration of the COR, the vertical displacement (2.9 ± 1.4 mm vs. 4.0 ± 1.1 mm, p = 0.016) and horizontal displacement (3.9 ± 2.4 mm vs. 5.3 ± 1.5 mm, p = 0.045) measured in the 3D-printed group were significantly smaller than those in the modular group. Additionally, the leg length discrepancy (3.1 ± 1.8 mm vs. 6.2 ± 2.9 mm, p < 0.001) and femoral offset difference (3.3 ± 2.2 mm vs.

5.1 ± 1.2 mm, $p = 0.006$) in the 3D-printed group were also significantly lower than those in the modular group (Table 3).

3.4. Biomechanical Results

3.4.1. Permanent Migration

Under cyclic loading, permanent migration of the modular cup–bone interface increased from 48 (48–55) μm at 200 cycles to 181 (178–186) μm at 800 cycles, and that of the augment–bone interface from 38 (35–41) to 135 (125–140) μm; in contrast, migration of the 3D-printed monoblock prosthesis interface remained below 95 μm throughout the test (86 [82–94] μm at 800 cycles) (Table S5; Fig. 6). Linear mixed-effects modeling showed that permanent migration was significantly smaller for the 3D-printed interface than for the modular cup–bone interface (group effect: β = −71.95 μm, 95% CI − 78.88 to − 65.02, $p < 0.001$), and that the between-group difference widened with increasing cycle number, from 14 μm at 200 cycles to 95 μm at 800 cycles (group × cycle interaction: β = −13.21 μm per 100 cycles, 95% CI − 16.31 to − 10.11, $p < 0.001$; Cohen's d = 10.0 at 800 cycles). The two-sided Wilcoxon signed-rank exact test on the within-specimen differences at 800 cycles showed the same direction of effect (exact $p = 0.0625$, the minimum achievable value at n = 5).

Finite element analysis yielded interfacial micromotion of 51 and 85 μm at 500 N and 840 N, respectively, for the 3D-printed design, versus 85 and 143 μm for the modular design (Fig. 6). These values were obtained from a single representative specimen and were therefore not subjected to statistical testing.

3.4.2. Inducible Micromotion

Across the loading cycles, micromotion of the modular augment–bone interface ranged from 95 to 175 μm under the 50–500 N load and from 167 to 240 μm under the 84–840 N load, while that of the cup–bone interface ranged from 165 to 236 μm and 175 to 334 μm under the two loads, respectively. The 3D-printed monoblock prosthesis interface remained at 79–95 μm and 111–126 μm under the two loads, respectively (Table S6). Linear mixed-effects modeling showed that inducible micromotion was significantly lower for the 3D-printed monoblock prosthesis throughout the 800-cycle protocol (group effect: β = −113.75 μm, 95% CI − 126.88 to − 100.61, $p < 0.001$, Cohen's d = 3.35). Descriptively, the median between-group difference widened from 103 μm (cycles 50–600) to 120 μm (cycles 650–800), although the group × cycle stage interaction was not significant (β = −9.00, 95% CI − 35.25 to 17.25, $p = 0.502$). The two-sided Wilcoxon signed-rank exact test showed the same direction of effect (exact $p = 0.0625$).

3.4.3. Strain Distribution

Under the 50–500 N load, the median values of peak compressive strains produced by the modular group at measurement points 1, 2, and 3 were 38.23, 231.69, and 276.22 με, respectively, while the 3D-printed group produced consistently higher compressive strains of 184.57, 301.23, and 452.32 με,

respectively. In terms of tensile strains, the values at the three measurement points for the modular prosthesis were 76.23, 186.79, and 119.72 με, respectively, while those for the 3D-printed group were 103.89, 214.56, and 88.68 με, respectively. Under the higher load of 84–840 N, this trend became more pronounced: the median values of peak compressive strains at measurement points 1, 2, and 3 for the modular group were 47.96, 369.24, and 428.82 με, respectively, while those for the 3D-printed group reached 334.76, 589.06, and 908.87 με, respectively. The median values of peak tensile strains for the modular group were 139.89, 303.32, and 190.06 με, respectively, while those for the 3D-printed group were 196.50, 375.55, and 166.08 με, respectively (Table S7; Fig. S4).

Finite element analysis revealed that peak stresses in both prostheses were concentrated at the contact interface with the acetabular cortical bone (Fig. 6). The 3D-printed monoblock prosthesis exhibited peak von Mises stresses of 23.7 MPa and 39.8 MPa under 500 N and 840 N, respectively, compared with 23.9 MPa and 40.4 MPa for the commercial modular acetabular prostheses.

4. Discussion

This study compared the clinical outcomes of patient-specific 3D-printed monoblock and commercial modular acetabular prostheses for the reconstruction of severe acetabular bone defects and independently evaluated their biomechanical behavior using cadaveric testing and FEA. Clinically, the monoblock prostheses were associated with better hip function, less postoperative pain, and more accurate restoration of the hip center of rotation. Biomechanically, the monoblock prostheses showed improved initial stability and more favorable periacetabular load transfer than commercial modular acetabular prostheses. Together, these concordant findings support the monoblock design as a promising option for reconstructing complex acetabular defects.

Commercial modular acetabular reconstruction systems, such as metal augments combined with acetabular cups, provide modular solutions for managing bone defects and have been widely used in clinical practice. However, their inherent limitations become evident when dealing with severe, irregular, or non-contained bone defects [22]. The standardized geometric shape of the augments is fixed, making it difficult to perfectly match individualized, varied bone defects, which leads to limited contact area between the augment and the host bone. Particularly when managing complex, large acetabular bone defects, multiple augments are often required, which not only increases the number of connections between prostheses, but also introduces inherent risks associated with modular structures, such as prosthesis interface wear [23]. This intraoperative passive adaptation strategy often leads to increased surgical difficulty and reduced initial stability of the prosthesis and has a negative impact on its long-term biological fixation. During surgery, standard augments often require secondary reaming to maximize bone contact, and intraoperative estimates suggest the shell ultimately contacts only 25%–30% of autogenous host bone in many cases, with the remainder against the augment or morselized allograft [24].

These intraoperative challenges translate into a substantial postoperative complication burden. Mid- to long-term series of commercial modular acetabular prostheses have reported complication rates of 32.7%–38.7% and re-revision rates of 11%–20.2% [25–27]. The risk is greatest in the most demanding scenario: in patients with pelvic discontinuity, the aseptic loosening rate of commercial modular acetabular prostheses reaches 60.0% [28].

To explore potential biomechanical mechanisms underlying these clinical challenges, we conducted biomechanical tests on cadaveric pelves. Under cyclic loading, commercial modular acetabular prostheses exhibited significant permanent migration and inducible micromotion, and this instability increased with the number of cycles and load levels. Such interface micromotion has been proposed to hinder bone ingrowth, promote fibrous tissue formation, and ultimately lead to aseptic loosening [9]. Beyond interface instability, compressive strain on the acetabulum in the modular group was consistently lower than that beneath the 3D-printed monoblock prosthesis at both load levels, and the difference became more pronounced as the load increased. Localized strain measurements alone cannot confirm global stress distribution, but the finite element analysis provided a complementary perspective: stress around the modular acetabulum was concentrated and unevenly distributed, indicating less homogeneous load transfer, whereas the monoblock prosthesis distributed loads more uniformly. This pattern is biomechanically coherent with the locally reduced periacetabular strain observed experimentally and suggests a propensity for stress shielding in the modular construct. Consistent with these findings, finite element analyses have shown that 3D-printed monolithic prostheses restore stress transmission close to that of native bone, whereas modular constructs exhibit marked stress concentration at the implant bone interface[29]. These findings align with the higher complication rates reported for commercial modular acetabular prostheses in clinical studies and offer a plausible mechanistic rationale.

Three-dimensional printing enables fabrication of a monoblock acetabular prosthesis that overcomes several limitations of commercial modular acetabular prostheses. First, prostheses manufactured from high-resolution preoperative CT data closely match the morphology of individual bone defects, which facilitates intraoperative fitting and eliminates trial-and-error component selection [30]; such defect-specific conformity also provides the geometric prerequisite for reliable initial stability. Second, the monoblock design eliminates micromotion at modular junctions, and the resulting stable interface provides a favorable environment for bone integration. Retrieval analyses have shown substantially greater bone ingrowth in 3D-printed monoblock prostheses than in commercial modular acetabular prostheses (median bone ingrowth area 65.7% vs. 33.9%; direct bone–implant contact 58.8% vs. 20.0%; ingrowth depth 60.0% vs. 5.7% of the porous layer) [31].

At the clinical level, these advantages are supported by favorable mid-term clinical outcomes: no re-revision, aseptic loosening, or osteolysis was observed in 23 patients at a mean follow-up of 4.7 years [8], and prosthesis survival was 100% at a mean of 3.3 years [14]. The biomechanical findings of the present study provide supporting evidence for these clinical observations. Under cyclic loading, migration of the commercial modular acetabular prostheses increased sharply with increasing load and

cycle number, whereas migration and micromotion at the monoblock interface remained consistently low—less than half those at the modular cup–bone interface and below the threshold of approximately 150 μm generally considered compatible with bone ingrowth. These findings can be attributed to two factors: CT-based anatomical matching maximizes prosthesis–host-bone contact and press-fit stability, and the monoblock design eliminates the modular junction and its associated micromotion, wear, and corrosion.

Beyond these macroscopic advantages, the 3D-printed monoblock prosthesis is also favorable in terms of biomechanical compatibility at the material and interface level. The porous metal structure not only enhances initial stability through a high friction coefficient, but also helps reduce stress shielding because its elastic modulus is close to that of bone [32–36]. Finite element comparisons have similarly shown lower contact stress and smaller relative micromotion for 3D-printed monoblock prostheses than for commercial modular acetabular prostheses, with contact stress and peak micromotion consistently lower under identical loads [37]. In our cadaveric tests, periacetabular strain was higher in the 3D-printed monoblock prosthesis at the measured locations, indicating more homogeneous load transfer and a lower propensity for stress shielding. Taken together, these findings suggest that the more uniform mechanical environment afforded by the 3D-printed monoblock prosthesis may support physiological bone remodeling at the interface.

The favorable clinical outcomes are consistent with these biomechanical advantages of patient-specific monoblock designs. With the aid of preoperative computer-aided design and finite element analysis, clinicians can prospectively plan key parameters such as the COR, abduction angle, and anteversion angle, thereby maximizing the restoration of the normal biomechanical environment of the hip joint [38]. In this study, the monoblock prostheses restored the COR, limb length, and offset more accurately—a direct manifestation of this "virtual rehearsal" type of planning. Because leg length and offset also depend on the femoral side, these differences likely reflect, at least in part, the accuracy of acetabular reconstruction. Accurate restoration of the COR preserves the tension balance of the periarticular soft tissues, reduces joint contact stress, and improves gait function, which is consistent with the higher HHS and lower VAS observed in this group.

Several limitations should be acknowledged. First, the retrospective design and relatively small cohort may limit generalizability. Because treatment allocation was based on shared surgeon–patient decision-making rather than randomization, residual selection bias and confounding by indication cannot be excluded. Second, the mean follow-up of approximately 32 months was insufficient to evaluate long-term implant survivorship and late complications. Follow-up of this cohort is ongoing, and longer-term outcomes will be reported when sufficient follow-up data become available. Third, the biomechanical analysis included only five cadaveric specimens and was limited to short-term cyclic loading. Moreover, because the clinical, cadaveric, and finite-element analyses were conducted independently, the observed findings should not be interpreted as definitive evidence of a direct mechanistic relationship among these levels of analysis.

5. Conclusion

Patient-specific 3D-printed monoblock acetabular prostheses were associated with better clinical outcomes, more accurate anatomical reconstruction, and improved initial stability compared with commercial modular acetabular prostheses. Long-term survivorship remains to be determined.

Declarations

Competing interests

We declare that we do not have any commercial or associative interest that represents a conflict of interest in connection with the work submitted.

Author Contributions

Conceptualization: CT, XYX and ZWD. Data curation: PRW, ZWD and ZCC. Formal analysis: ZWD, XYX and PRW. Investigation: BC, WHZ, WHH, MTW and PRW. Methodology: CT, PRW and XYX. Validation: ZWD, XYX, WHZ, BC. Writing – original draft: ZWD. Writing – review & editing: CT, PRW and ZWD. Final approval of the article: CT, LMW. All authors contributed to the article and approved the submitted version.

Funding

This study was supported by the National Key Research and Development Program of China (2023YFB3813000), Nanjing Medical Science and Technology Development Foundation (ZKX22032).

Ethics approval and consent to participate

This study was performed in line with the principles of the Declaration of Helsinki and was reviewed and approved by the Ethics Committee of Nanjing First Hospital (Approval No. KY20240514-09-KS-01; approval date: 3 June 2024). The clinical component involved the retrospective analysis of previously collected clinical, imaging, operative, and follow-up data. Written informed consent was obtained from all patients included in the retrospective clinical component. The five formalin-fixed human pelvis specimens used in the biomechanical component were provided by the Department of Human Anatomy, Nanjing Medical University, from bodies donated to the university for teaching and research. Written informed consent authorizing the use of the bodies for medical education and scientific research had been obtained from the donors themselves or, where applicable, their legally authorized representatives, in accordance with applicable institutional procedures. All specimens were anonymized or deidentified before being provided to the research team, and the researchers had no access to personally identifiable donor information. The procurement, preservation, management, and scientific use of the specimens complied with applicable institutional and national ethical requirements.

Consent for publication

Not applicable.

Acknowledgments

The authors are grateful to b-ONE ORTHO, Corp. and Beijing Chunlizhengda Medical Instruments Co., Ltd. for their unrestricted donation of the acetabular prostheses for the biomechanical tests in this research, and LetPub (www.letpub.com.cn) for its linguistic assistance during the preparation of this manuscript.

Availability of data and materials

The data supporting the findings of this study are available from the corresponding author upon reasonable request.

References

1. Fahmy M, Karim MA, Abo-Elsoud M, Shawky MA. Single trabecular titanium Cup-Cage for acetabular bone defects during revision hip arthroplasty: Mid-term outcomes. J Orthop Surg Res. 2025;20:1087. https://doi.org/10.1186/s13018-025-06553-x.
2. Paprosky WG, Burnett RSJ. Assessment and classification of bone stock deficiency in revision total hip arthroplasty. Am J Orthop (Belle Mead NJ). 2002;31:459–64.
3. Wang Q, Wang Q, Liu P, Ge J, Zhang Q, Guo W, et al. Clinical and radiological outcomes of jumbo cup in revision total hip arthroplasty: A systematic review. Front Surg. 2022;9:929103. https://doi.org/10.3389/fsurg.2022.929103.
4. Sershon RA, Sheth NP, Hartzler MA, Levine BR. Pelvic Reconstruction for Complex Bone Defects in Revision Total Hip Arthroplasty. J Arthroplasty. 2025;40:S41–8. https://doi.org/10.1016/j.arth.2025.04.055.
5. Sculco PK, Wright T, Malahias M-A, Gu A, Bostrom M, Haddad F et al. The Diagnosis and Treatment of Acetabular Bone Loss in Revision Hip Arthroplasty: An International Consensus Symposium. HSS J Musculoskelet J Hosp Spec Surg. 2022;18:8–41. https://doi.org/10.1177/15563316211034850
6. Zhou B, Chan PK, Wang D. The utilisation of porous metal augments for acetabular reconstruction during revision total hip arthroplasty. Hip Int. 2026;36:151–63. https://doi.org/10.1177/11207000251385230.
7. Cimatti P, Del Piccolo N, Mazzotta A, Dallari B, Pennello E, Dallari D. Use of structural bone allograft in revision hip arthroplasty for massive acetabular defect: A systematic review and meta-analysis. J Exp Orthop. 2025;12:e70241. https://doi.org/10.1002/jeo2.70241.
8. Kong K, Zhao C, Chang Y, Qiao H, Hu Y, Li H, et al. Use of Customized 3D-Printed Titanium Augment With Tantalum Trabecular Cup for Large Acetabular Bone Defects in Revision Total Hip Arthroplasty: A Midterm Follow-Up Study. Front Bioeng Biotechnol. 2022;10:900905. https://doi.org/10.3389/fbioe.2022.900905.
9. Wang Y, Wang M, Li C, Nakamura Y, Deng L, Yamako G, et al. Biomechanical effect of metal augment and bone graft on cup stability for acetabular reconstruction of total hip arthroplasty in hip

dysplasia: a finite element analysis. BMC Musculoskelet Disord. 2022;23:277. https://doi.org/10.1186/s12891-022-05168-1.

10. Cassar-Gheiti AJ, Mei XY, Afenu EA, Safir OA, Gross AE, Kuzyk PRT. Midterm Outcomes After Reconstruction of Superolateral Acetabular Defects Using Flying Buttress Porous Tantalum Augments During Revision Total Hip Arthroplasty. J Arthroplasty. 2021;36:2936–41. https://doi.org/10.1016/j.arth.2021.03.040.
11. Pandey AK, Zuke WA, Surace P, Kamath AF. Management of acetabular bone loss in revision total hip replacement: a narrative literature review. Ann Jt. 2024;9:21. https://doi.org/10.21037/aoj-23-23.
12. Chaudhry F, Daud A, Greenberg A, Braunstein D, Safir OA, Gross AE, et al. Cup-Cage Construct for Treatment of Severe Acetabular Bone Loss in Revision Total Hip Arthroplasty: Clinical and Radiographic Outcomes at a Mean Follow-Up of 7.7 Years. J Arthroplasty. 2024;39:2555–60. https://doi.org/10.1016/j.arth.2024.07.010.
13. Durand-Hill M, Henckel J, Di Laura A, Hart AJ. Can custom 3D printed implants successfully reconstruct massive acetabular defects? A 3D-CT assessment. J Orthop Res Off Publ Orthop Res Soc. 2020;38:2640–8. https://doi.org/10.1002/jor.24752.
14. Ying J, Cheng L, Li J, Wu B, Qiu X, Zhang T, et al. Treatment of Acetabular Bone Defect in Revision of Total Hip Arthroplasty Using 3D Printed Tantalum Acetabular Augment. Orthop Surg. 2023;15:1264–71. https://doi.org/10.1111/os.13691.
15. Rana M, Karmakar S, Bandyopadhyay A, Roychowdhury A. Design and manufacturing of patient-specific Ti6Al4V implants with inhomogeneous porosity. J Mech Behav Biomed Mater. 2023;143:105925. https://doi.org/10.1016/j.jmbbm.2023.105925.
16. Perry J, Burnfield J. Gait Analysis: Normal and Pathological Function. 2nd ed. Boca Raton: CRC; 2024. https://doi.org/10.1201/9781003525592.
17. Bergmann G, Bender A, Dymke J, Duda G, Damm P. Standardized Loads Acting in Hip Implants. PLoS ONE. 2016;11:e0155612. https://doi.org/10.1371/journal.pone.0155612.
18. Beckmann NA, Bitsch RG, Schonhoff M, Siebenrock K-A, Schwarze M, Jaeger S. Comparison of the Primary Stability of Porous Tantalum and Titanium Acetabular Revision Constructs. Mater (Basel). 2020;13:1783. https://doi.org/10.3390/ma13071783.
19. Thomas KA, Vrahas MS, Noble JW, Bearden CM, Reid JS. Evaluation of hip stability after simulated transverse acetabular fractures. Clin Orthop Relat Res. 1997;340:244–56. https://doi.org/10.1097/00003086-199707000-00032.
20. Bergmann G, Graichen F, Rohlmann A, Bender A, Heinlein B, Duda GN, et al. Realistic loads for testing hip implants. Biomed Mater Eng. 2010;20:65–75. https://doi.org/10.3233/BME-2010-0616.
21. Du Y, Fu J, Sun J, Zhang G, Chen J, Ni M, et al. Acetabular Bone Defect in Total Hip Arthroplasty for Crowe II or III Developmental Dysplasia of the Hip: A Finite Element Study. Biomed Res Int. 2020;2020:4809013. https://doi.org/10.1155/2020/4809013.
22. Shi T, Zhang W, Fang X. Custom 3D-printed porous titanium augments for Paprosky type III acetabular defects: a case series combining biomechanical rationale with early clinical outcomes.

3D Print Med. 2025;11:41. https://doi.org/10.1186/s41205-025-00293-8.

23. Xiong C, Jing Z, Ni R, Yang Y, Meng D, Yang X, et al. Interfacial Strength Between Porous Metal Acetabular Components and Augments. JBJS Open Access. 2025;10. https://doi.org/10.2106/JBJS.OA.24.00245. e24.00245.
24. Siegmeth A, Duncan CP, Masri BA, Kim WY, Garbuz DS. Modular tantalum augments for acetabular defects in revision hip arthroplasty. Clin Orthop Relat Res. 2009;467:199–205. https://doi.org/10.1007/s11999-008-0549-0.
25. Babis GC, Sakellariou VI, Chatziantoniou AN, Soucacos PN, Megas P. High complication rate in reconstruction of Paprosky type IIIa acetabular defects using an oblong implant with modular side plates and a hook. J Bone Joint Surg Br. 2011;93:1592–6. https://doi.org/10.1302/0301-620X.93B12.27299.
26. Braunstein D, Greenberg A, Chaudhry F, Daud A, Safir OA, Gross AE, et al. Acetabular Augments Used in Revision Hip Arthroplasty: Minimum 10-year Follow-Up of Implant Survivorships, Functional Scores, and Radiographic Outcomes. J Arthroplasty. 2025;40:751–7. https://doi.org/10.1016/j.arth.2024.09.004.
27. Spranz D, Müller L-M, Trefzer R, Hetto P, Nees T, Walker T, et al. Mid-term results of reconstruction rings used in combination with modular tantalum augments for Paprosky type III acetabular defects in revision hip arthroplasty. J Exp Orthop. 2025;12:e70489. https://doi.org/10.1002/jeo2.70489.
28. Tikhilov RM, Dzhavadov AA, Kovalenko AN, Bilyk SS, Denisov AO, Shubnyakov II. Standard Versus Custom-Made Acetabular Implants in Revision Total Hip Arthroplasty. J Arthroplasty. 2022;37:119–25. https://doi.org/10.1016/j.arth.2021.09.003.
29. Hu X, Wen Y, Lu M, Luo Y, Zhou Y, Yang X, et al. Biomechanical and clinical outcomes of 3D-printed versus modular hemipelvic prostheses for limb-salvage reconstruction following periacetabular tumor resection: a mid-term retrospective cohort study. J Orthop Surg Res. 2024;19:258. https://doi.org/10.1186/s13018-024-04697-w.
30. Cheng L, Liu Y, Wang L, Ying J, Li J, Wang F, et al. Integrated Acetabular Prosthesis Versus Bone Grafting in Total Hip Arthroplasty for Crowe Type II and III Hip Dysplasia: A Retrospective Case-Control Study. Orthop Surg. 2024;16:2401–9. https://doi.org/10.1111/os.14143.
31. Dall'Ava L, Hothi H, Henckel J, Di Laura A, Tirabosco R, Eskelinen A, et al. Osseointegration of retrieved 3D-printed, off-the-shelf acetabular implants. Bone Jt Res. 2021;10:388–400. https://doi.org/10.1302/2046-3758.107.BJR-2020-0462.R1.
32. Guo F, Huang S, Hu M, Yang C, Li D, Liu C. Biomechanical evaluation of a customized 3D-printed polyetheretherketone condylar prosthesis. Exp Ther Med. 2021;21:348. https://doi.org/10.3892/etm.2021.9779.
33. Faldini C, Mazzotti A, Belvedere C, Durastanti G, Panciera A, Geraci G, et al. A new ligament-compatible patient-specific 3D-printed implant and instrumentation for total ankle arthroplasty: from biomechanical studies to clinical cases. J Orthop Traumatol. 2020;21:16. https://doi.org/10.1186/s10195-020-00555-7.

34. Liu B, Lv Y, Li X, Liu Z, Zheng Y, Wen P, et al. Influence of different fixation modes on biomechanical conduction of 3D printed prostheses for treating critical diaphyseal defects of lower limbs: A finite element study. Front Surg. 2022;9:959306. https://doi.org/10.3389/fsurg.2022.959306.
35. Bagheri A, Buj-Corral I, Ferrer M, Pastor MM, Roure F. Determination of the Elasticity Modulus of 3D-Printed Octet-Truss Structures for Use in Porous Prosthesis Implants. Mater (Basel). 2018;11:2420. https://doi.org/10.3390/ma11122420.
36. Liverani E, Rogati G, Pagani S, Brogini S, Fortunato A, Caravaggi P. Mechanical interaction between additive-manufactured metal lattice structures and bone in compression: implications for stress shielding of orthopaedic implants. J Mech Behav Biomed Mater. 2021;121:104608. https://doi.org/10.1016/j.jmbbm.2021.104608.
37. Liu Y, Wang F, Ying J, Xu M, Wei Y, Li J, et al. Biomechanical analysis and clinical observation of 3D-printed acetabular prosthesis for the acetabular reconstruction of total hip arthroplasty in Crowe III hip dysplasia. Front Bioeng Biotechnol. 2023;11:1219745. https://doi.org/10.3389/fbioe.2023.1219745.
38. Wang Z, Wang Z, Gu L, Zhang Y, Su T, Luo J, et al. 3D-printed porous tantalum for acetabular reconstruction in complex primary arthroplasty and revision of hip. Front Bioeng Biotechnol. 2025;13:1557882. https://doi.org/10.3389/fbioe.2025.1557882.

Figures

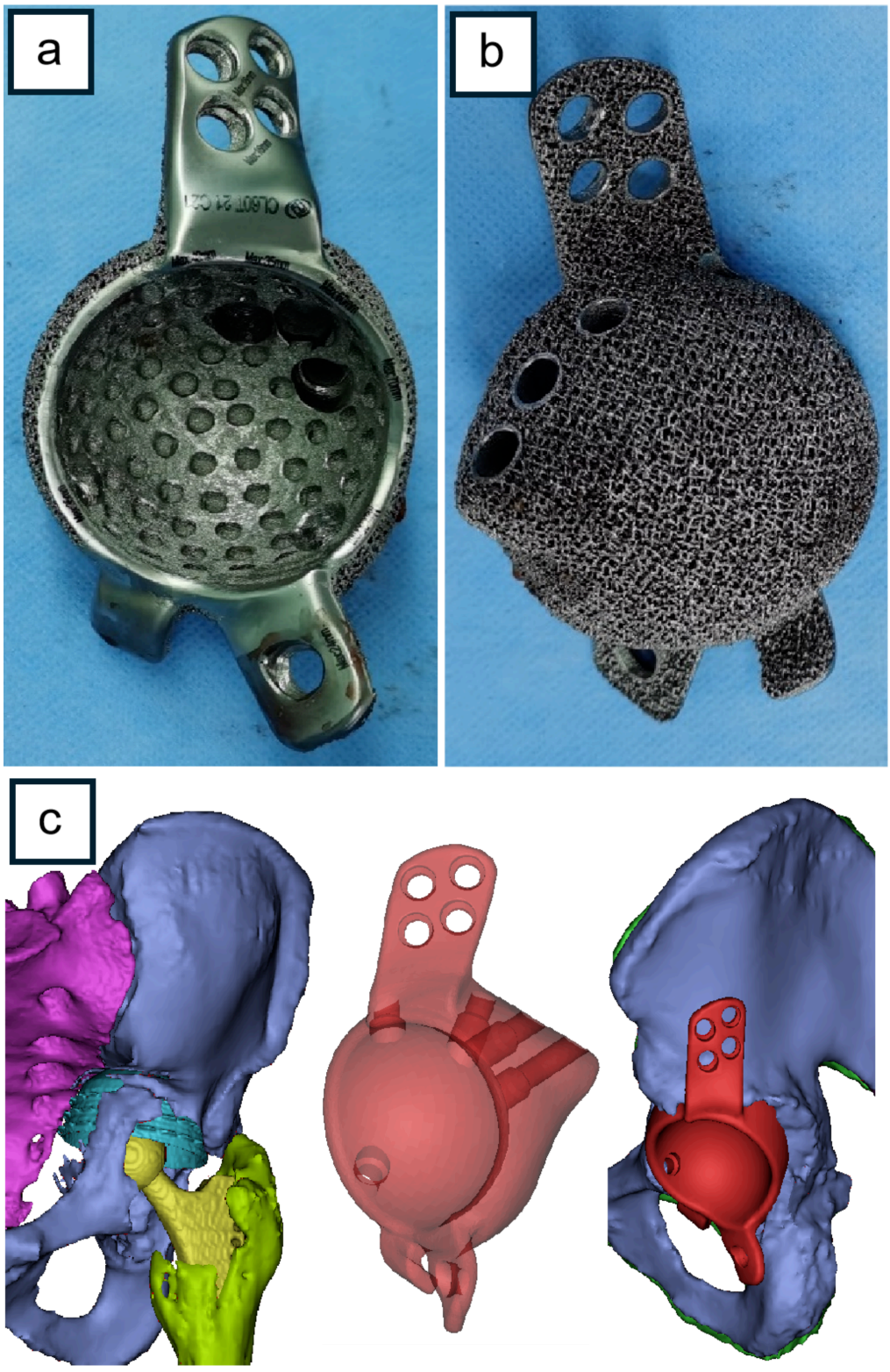


Figure 1

Patient-specific 3D-printed monoblock acetabular prosthesis and design for a Paprosky IIIB defect.**a, b** Anterior and posterior views of the 3D-printed monoblock prosthesis, illustrating its custom design for a severe acetabular defect. **c** Preoperative three-dimensional planning and prosthesis design

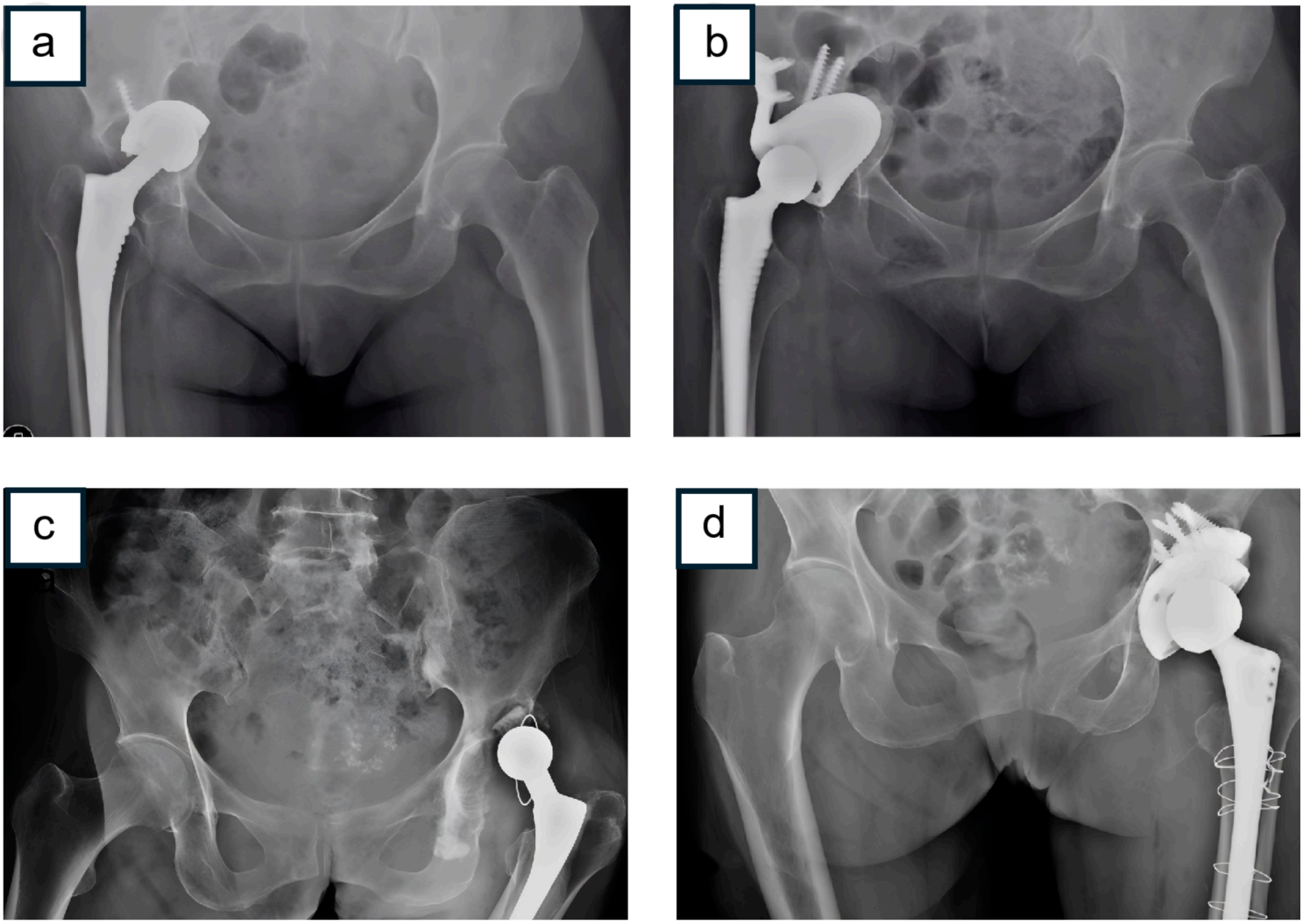


Figure 2

Representative preoperative and postoperative radiographs comparing two reconstruction methods.**a, b** A Paprosky type IIIB acetabular defect treated with a 3D-printed monoblock prosthesis: **a** Preoperative view; **b** Postoperative view. **c, d** A Paprosky type IIIA acetabular defect treated with commercial modular acetabular prostheses: **c** Preoperative view; **d** Postoperative view

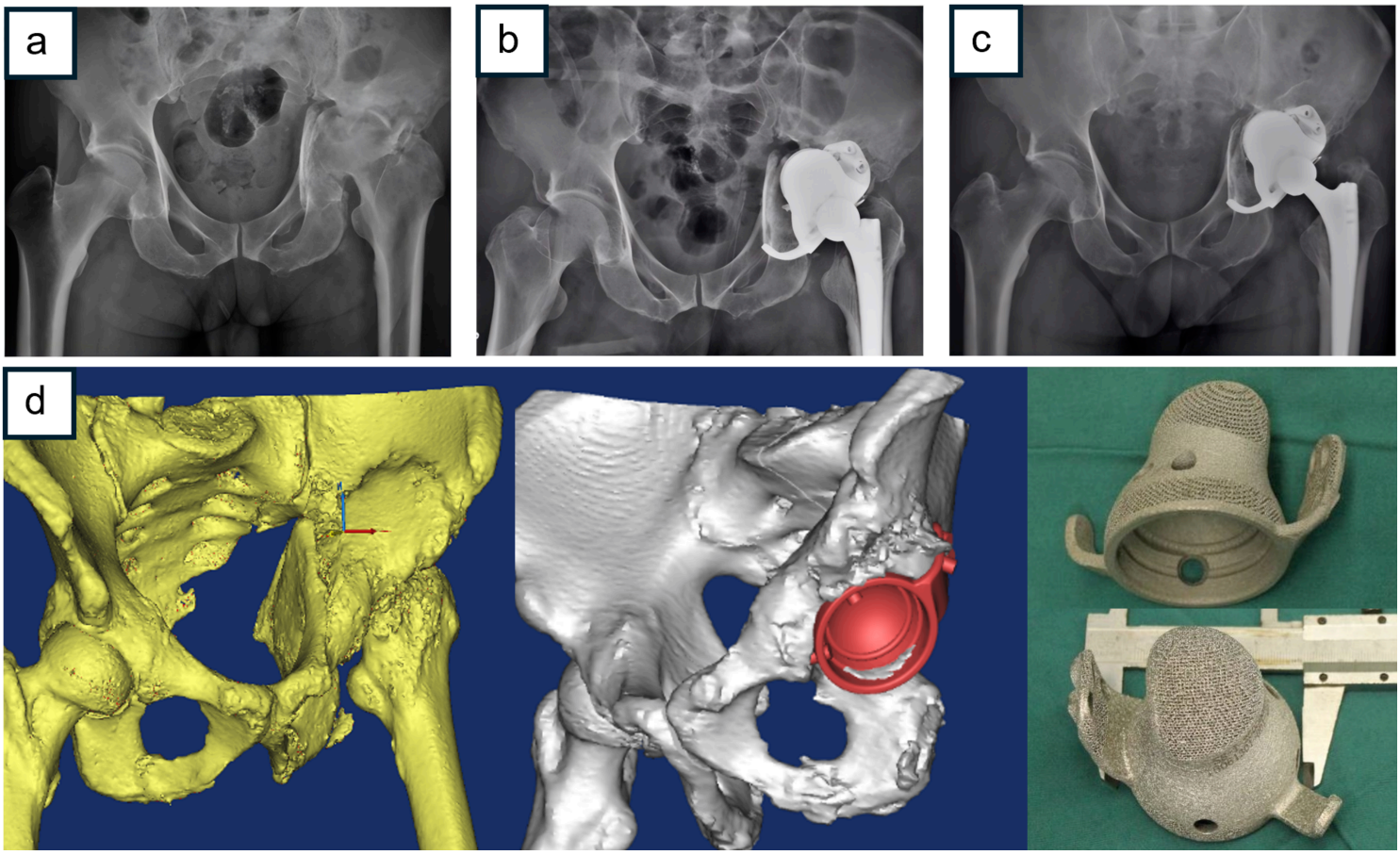


Figure 3

Preoperative design and radiographic outcomes of 3D-printed monoblock acetabular reconstruction for a Paprosky IIIB defect. **a** Preoperative radiograph demonstrating the severe acetabular bone loss and compromised hip center. **b**Immediate postoperative radiograph showing the 3D-printed monoblock prosthesis in situ with satisfactory restoration of the hip center of rotation. **c**Radiograph at the final 45-month follow-up, confirming stable prosthesis fixation with no signs of loosening, migration, or osteolysis. **d**Preoperative design workflow and the finalized prosthesis

Image not available with this version

Figure 4

Cadaveric specimen preparation, defect creation, and prosthesis implantation. A representative specimen is shown. **a, b, c** Sequential images showing the creation of a standardized Paprosky type IIIA defect and implantation of commercial modular acetabular prostheses in the right hemipelvis. **d, e, f** Corresponding sequential images for the creation of an identical defect and implantation of a 3D-printed monoblock prosthesis in the left hemipelvis. **g, h** Post-creation radiographic verification of the defects using 3D computed tomography (CT) reconstruction and an anteroposterior (AP) pelvic radiograph, confirming the symmetry of the created defects. **i** Final postoperative AP radiograph of the entire specimen, demonstrating the final position of both the modular and 3D-printed components

Figure 5

Overview of the biomechanical testing methodology. **a** The pelvis specimens were fixed in the custom mechanical testing rig. **b** Illustration of the measurement setup, showing optical markers for tracking interface micromotion and strain gauges for measuring acetabular bone strain. **c** A schematic diagram illustrating the two-stage cyclic loading profile applied to simulate partial weight-bearing conditions, depicting the progression from low to high magnitude ranges rather than actual experimental recordings

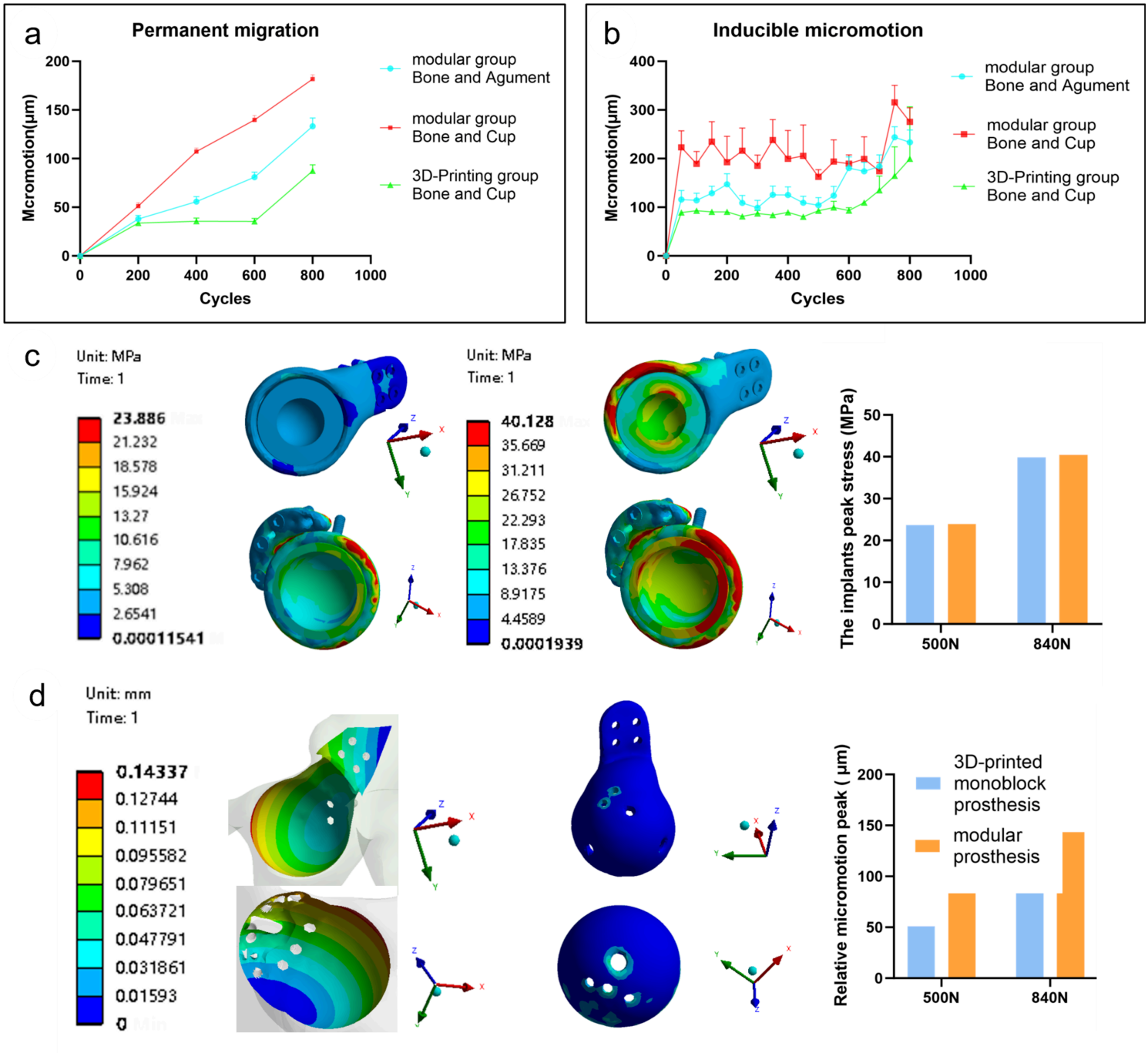


Figure 6

Biomechanical evaluation of interface stability and acetabular strain. **a, b** Cadaveric biomechanical testing: **a** Permanent migration (initial subsidence) at the bone–prosthesis interface following cyclic loading; **b** Maximum inducible micromotion at the bone–prosthesis interface during cyclic loading. **c, d**Finite element analysis: **c** Peak prosthetic stress under the two loading protocols; **d** Relative micromotion at the prosthesis–bone interface for both prosthetic designs under the two loading protocols

Supplementary Files

This is a list of supplementary files associated with this preprint. Click to download.

- SupplementarymaterialsTablesandFigures.docx